**Title:** Optimizing aerial imagery collection and processing parameters for drone-based individual tree mapping in structurally complex conifer forests

**Authors:**

Derek J. N. Young*; Department of Plant Sciences, University of California, Davis, CA 95616

Michael J. Koontz; Earth Lab, University of Colorado, Boulder, CO 80303

JonahMaria Weeks; Department of Environmental Science and Policy, University of California, Davis, CA 95616

*Corresponding author. Email address: djyoung@ucdavis.edu

**Running head:** Drone-based individual tree mapping

**Abstract:**

1: Recent advances in remotely piloted aerial systems (“drones”) and imagery processing enable individual tree mapping in forests across broad areas with low-cost equipment and minimal ground-based data collection. One such method involves collecting many partially overlapping aerial photos, processing them using “structure from motion” (SfM) photogrammetry to create a digital 3D representation, and using the 3D model to detect individual trees. SfM-based forest mapping involves myriad decisions surrounding methods and parameters for imagery acquisition and processing, but it is unclear how these individual decisions or their combinations impact the quality of the resulting forest inventories.

2: We collected and processed drone imagery of a moderate-density, structurally complex mixed-conifer stand. We tested 22 imagery collection methods (altering flight altitude, camera pitch, and image overlap), 12 imagery processing parameterizations (image resolutions and depth map filtering intensities), and 286 tree detection methods (algorithms and their parameterizations) to create 7,568 tree maps. We compared these maps to a 3.23-ha ground reference map of 1,775 trees > 5 m tall that we created using traditional field survey methods.

3: The accuracy of individual tree detection (ITD) and the resulting tree maps was generally maximized by collecting imagery at high altitude (120 m) with at least 90% image-to-image overlap, photogrammetrically processing images into a canopy height model (CHM) with a 2-fold upscaling (coarsening) step, and detecting trees from the CHM using a variable window filter after applying a moving-window mean smooth to the CHM. Using this combination of methods, we mapped trees with an accuracy exceeding expectations for structurally complex forests (for overstory trees > 10 m tall, sensitivity = 0.69 and precision = 0.90). Remotely measured tree

heights corresponded to ground-measured heights with $R^2$ = 0.95. Accuracy was higher for taller trees and lower for understory trees, and would likely be higher in less dense and less structurally complex stands.

4: Our results may guide others wishing to efficiently produce broad-extent individual-tree maps of conifer forests without investing substantial time tailoring imagery acquisition and processing parameters. The resulting tree maps create opportunities for addressing previously intractable ecological questions and informing forest management.

**Keywords:** Drone, inventory, map, photogrammetry, remote sensing, structure-from-motion, tree, UAV

## Introduction

Forest inventories characterize the species, size, condition, and location of individual trees and are critical resources for advancing ecological theory and informing forest management (Hubbell et al., 1999; Lasky et al., 2014; North et al., 2021; Whittaker, 1956; Wright et al., 2010; Young et al., 2020). Forest inventories are traditionally completed by ground-based field crews and require substantial time, labor, and financial investment, which limits their spatial extent and continuity (Gray et al., 2012; USDA Forest Service, 2016). To address these constraints, forest mapping approaches have more recently employed remote sensing data to create continuous forest inventories over broad areas. Remote sensing-based forest mapping has traditionally taken an “area-based” approach in which remote sensing data (e.g., spectral reflectance data from satellite or aerial imagery) are used to estimate forest summary statistics such as tree density, mean tree height, and aboveground biomass (De Luca et al., 2019; Jayathunga et al., 2018; Lamping et al., 2021; Puliti et al., 2019; Rodman et al., 2019). However, the increasing quality of remote sensing data and processing workflows has recently enabled remote forest mapping more analogous to field-based approaches that involve detecting and characterizing individual trees (Jeronimo et al., 2018; Koontz et al., 2021; Swayze et al., 2021).

Small remotely piloted aerial systems (RPAS, or “drones”) provide data at a scale particularly well suited for individual tree detection (ITD). A fundamental technique in drone-based forest mapping involves collecting many partially overlapping images in a dense grid over the study area. The images are supplied to a photogrammetry algorithm, which employs principles of perspective and triangulation to estimate the 3D structure of the landscape by quantifying the amount by which landscape features move relative to each other between images. This method is commonly referred to as “structure from motion” (SfM; Dandois & Ellis, 2013; Iglhaut et al., 2019; Westoby et al., 2012) because the many optical perspectives from the drone as it moves allows modeling of the 3D structure of objects and landscapes. The

structure data can be represented as a point cloud in which each point identifies a surface (e.g., leaf, stem, ground) that appears in multiple photos. The point cloud data can be processed into raster-format vegetation canopy height models (CHMs).

SfM-derived point cloud data share many characteristics with point clouds derived from aerial light detection and ranging (lidar; also known as aerial laser scanning, ALS), which can also be used for ITD (Jeronimo et al., 2018; Zaforemska et al., 2019) and may better capture sub-canopy structure because some laser pulses penetrate the canopy (Jayathunga et al., 2018; Lamping et al., 2021; Lisein et al., 2013). Because ALS-derived point clouds have historically been collected using crewed aircraft flying higher than a typical drone operation, they generally cover more ground area per mission but have substantially reduced resolution and point density (e.g., < 10 points $m^{-2}$; USGS, 2018; Weinstein et al., 2021) compared to drone-based SfM point clouds (e.g., > 100 points $m^{-2}$, this study). Technological advances have enabled drone-mounted lidar instrumentation that can achieve a density of thousands of points $m^{-2}$ (Kellner et al., 2019; Lin et al., 2011; Sankey et al., 2017). In comparison to drone-mounted lidar, however, drone-based SfM data is much less costly to obtain (it can be collected with standard RGB [red, green, blue] cameras) and can be collected over moderately-sized focal areas with high frequency and minimal advance planning (Camarretta et al., 2020; Mlambo et al., 2017).

Numerous algorithms have been developed to detect individual trees from CHMs (e.g., Popescu & Wynne, 2004) and directly from point clouds (e.g., Li et al., 2012; Xiao et al., 2019). ITD accuracy varies considerably depending on the stand structural characteristics and algorithms used, with higher accuracy in lower-density stands and in overstory vs. understory trees. ITD accuracy is arguably best summarized using the F score, which incorporates the rates of both correct and false positive detections. The F score is calculated as the harmonic mean of the sensitivity (proportion of ground reference trees detected; also called recall) and the

precision (proportion of detected trees that match ground reference trees) and ranges between 0 (no ground trees detected) and 1 (all ground trees detected and no false positive detections).

$$sensitivity = \frac{n_{ground\_trees\_matching\_drone\_trees}}{n_{ground\_trees}}$$

$$precision = \frac{n_{drone\_trees\_matching\_ground\_trees}}{n_{drone\_trees}}$$

$$F\ score = \frac{2}{\frac{1}{sensitivity} + \frac{1}{precision}} = 2 \cdot \frac{sensitivity \cdot precision}{sensitivity + precision}$$

Recent ITD work using drone-derived SfM products for overstory trees (Creasy et al., 2021; Mohan et al., 2017) or for all trees in low- to moderate-density stands (Belmonte et al., 2020; Bonnet et al., 2017; Swayze et al., 2021) has obtained F scores ranging roughly between 0.75 and 0.85, whereas for higher-density stands or understory trees, performance tends to be lower (e.g., F < 0.65; Creasy et al., 2021). The height and canopy extent of automatically detected trees can usually be measured from CHM or point cloud data with high accuracy (RMSE: 3-7% and $R^2$ > 0.70; Belmonte et al., 2020; Creasy et al., 2021; Silva et al., 2016), though the narrow tops of standing dead trees can be missing in the 3D reconstruction, leading to underestimates of dead tree height (Koontz et al., 2021).

Despite the promise of drone-based tree mapping using SfM, relatively little work has quantitatively evaluated the influence of different imagery collection, imagery processing, and tree detection methods on the accuracy of the resulting tree maps. Using an oblique (as opposed to directly downward, or “nadir”) camera pitch can increase the accuracy of digital terrain models derived from drone images in areas with low vegetation cover (Nesbit & Hugenholtz, 2019) and in forests can increase the point cloud density in the lower canopy and understory (Díaz et al., 2020; Lamping et al., 2021). However, the only published evaluation of camera pitch specifically in the context of individual tree detection (ITD) found that tree detection accuracy was greater with a nadir vs. oblique camera pitch (Swayze et al., 2021). Flight (image collection) altitude may additionally affect 3D reconstruction quality, likely through

its effect on the spatial resolution of the resulting imagery (higher altitude results in coarser grain imagery) (Dandois et al., 2015). However, previous work has found little difference in ITD performance among flights conducted between 64 and 115 m above ground level (Swayze et al., 2021) and between 50 and 100 m above ground level (Torres-Sánchez et al., 2018). Finally, while increased image collection density (i.e., overlap) is associated with increased point cloud quality and density (Dandois & Ellis, 2013; Frey et al., 2018; Ni et al., 2018), it also increases image dataset size and acquisition and processing times. Increasing image overlap can increase ITD accuracy (Swayze et al., 2021), but it provides diminishing returns to accuracy at increasingly high overlap (Torres-Sánchez et al., 2018).

Image resolution and outlier filtering are key parameters that can be adjusted during the SfM processing. A strong understanding of photogrammetric analysis principles can provide key insights into how these parameters may be adjusted to yield more successful 3D reconstructions (Over et al., 2021; USGS, 2017), but empirical validation of these workflows in the context of forest inventories is generally lacking. Only one study to our knowledge has evaluated image resolution and point cloud filtering parameters in the context of ITD (Tinkham & Swayze, 2021). Using the Metashape v1.6.4 photogrammetry software (Agisoft, LLC), Tinkham & Swayze (2021) found that retaining maximal image resolution and minimizing outlier filtering during point cloud generation yielded the greatest ITD performance. However, this study did not evaluate the influence of image resolution during the alignment stage. Using full image resolution during processing may increase point cloud detail and density (Jayathunga et al., 2018; Lisein et al., 2013), but (a) higher resolution data can substantially increase processing times, (b) high-resolution images may be difficult to align and compare when they include small surfaces like leaves and branches that move or blow in the wind, and (c) the extent to which any increase in point cloud detail translates to improved ITD performance is not well known.

Finally, once photogrammetric products are generated, there are myriad options for ITD algorithm selection and parameterization. Several studies have compared the accuracy of

different ITD algorithms and/or parameterizations applied to SfM-derived canopy height models and point clouds. Mohan et al. (2017) tested 4 different parameterizations of a CHM-based fixed window filter, combined factorially with 4 different CHM smoothing intensities, for a total of 16 parameter sets. Creasy et al. (2021) evaluated 97 different parameterizations of a CHM-based variable- and fixed- window filtering method (Plowright, 2021). Shin et al. (2018) tested 16 parameterizations of a point cloud-based ITD algorithm (Li et al., 2012). Koontz et al. (2021) tested a total of 177 parameter sets across 7 different CHM- and point cloud-based ITD algorithms, identifying a parameterization of a point cloud-based method (Roussel, 2021b) as the most accurate. While it also included a test of a variable window filtering algorithm (Plowright, 2021), it tested only 3 parameter sets for this algorithm based on previous results from lidar acquisitions (Popescu and Wynne, 2004) and thus provides limited opportunity for comparison with previous studies that employed this method.

While work to date has quantified the influence of flight and photogrammetry parameters on the resulting photogrammetry products, few studies have evaluated how these parameters affect the accuracy of the forest inventory--the ultimate product that informs ecological inference and management decisions. Further, evaluations of SfM-based tree detection algorithms to date have generally not simultaneously considered the role of imagery collection and processing parameters that create the photogrammetry products. Evaluating the influence of these categories of variables jointly may allow detection of consistent effects vs. idiosyncrasies and may reveal important interactions that enable meaningful improvements in ITD accuracy and efficiency. In addition, many evaluations of ITD methods have been conducted in stands with relatively simple structure and low tree density, potentially yielding parameter selection and tree detection performance different than may be expected in higher-density, more structurally-complex stands. In the present study, we evaluate multiple factorial combinations of imagery collection parameters (flight altitude, camera pitch, and image overlap), imagery processing parameters (image resolution for image alignment and for dense cloud generation,

and point cloud outlier filtering intensity), and tree detection methods (algorithm and parameterization), for a total of 7,568 combinations, in a moderately dense, structurally complex mixed-conifer stand in the Sierra Nevada of California.

## Methods

### *Overview*

We created a ground reference tree map of 1,916 trees > 5 m tall in a 3.23-ha focal area using traditional survey methods. We also used automated algorithms to create 7,568 alternative tree maps for this area from aerial imagery collected by drone to evaluate the influence of image acquisition and processing parameters on aerial tree mapping accuracy. In Stage 1, we identified the best-performing photogrammetry processing processing parameters and automated tree detection methods. In Stage 2, we applied those methods to identify the best image acquisition parameters (flight altitude, image overlap, and camera pitch) (Fig. 1).

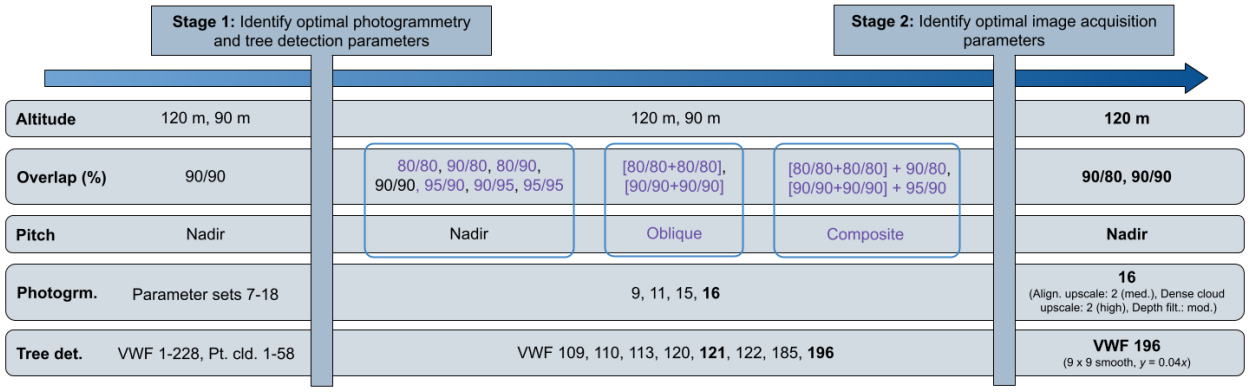


**Fig. 1:** The optimization workflow employed in this study. For each of the two optimization stages (vertical bars), the ranges of tested parameters appear on the left, and the ranges of selected parameters appear on the right *in black text*, with the best performing sets bolded. Additional parameters tested in Stage 2 that were not derived from Stage 1 results appear in purple text. For each optimization stage, all factorial combinations of parameters across each category (e.g., altitude, photogrammetry, and tree detection) were tested, except that only

certain pitch-overlap combinations were tested (factorial combinations within blue outlines). While Stage 2 revealed several parameter combinations with strong performance (see text), the right-hand side of the diagram shows the most consistently best (e.g., vwf_196 tree detection) and/or most practical (90/80 and 90/90 overlap; 120 m altitude) among comparably performing parameters. Thus, the rightmost column represents the “recommended” set of parameters for this forest type, based on our results. Front and side overlap values are given as percentages, in the format “front/side”. Overlap pairings in brackets (e.g., [90/90+90/90]) refer to the combination of N-S and E-W missions with oblique camera pitch. Oblique pairings are combined with nadir missions to create composite sets (e.g., [90/90+90/90] + 95/90). The vwf_196 tree detection parameterization is defined by the equation $y = 0.04x$ (depicted in parentheses in the figure’s bottom right cell), where $y$ is the radius of the search window for higher points centered on a focal point, and $x$ is the height of the focal point; this algorithm is applied to the CHM following a 9 x 9 pixel moving window mean smooth. Other tree detection parameter sets are defined in Appendix S2: Tables S1 and S2; photo sets are described in Table 2; and photogrammetry parameter sets are described in Table 3. Photogrm.: Photogrammetry parameterization; Tree det.: Tree detection algorithm; VWF = variable window filter; Pt. cld.: point cloud-based method.

*Focal area*

Our study site was a 3.23 ha area of mixed-conifer forest (Safford & Stevens, 2017) in Emerald Bay State Park on the shore of Lake Tahoe in the Sierra Nevada of California (Fig. 2a). The stand is co-dominated, in decreasing order of abundance, by ponderosa pine (*Pinus ponderosa*), incense cedar (*Calocedrus decurrens*), Jeffrey pine (*Pinus jeffreyi*), and white fir (*Abies concolor*). The stand has high structural complexity, with a continuous size distribution and small trees interspersed with larger trees and often underneath their canopies (Figs. 2b, 3). The topography is flat (elevation range: 1900 to 1905 m). We developed a 3.23-ha

ground-reference stand inventory by establishing a grid of points and measuring the distance (using a laser rangefinder) and azimuth (using a sighting compass) to each tree with diameter at breast height (DBH) > 7.5 cm from a nearby grid point (Appendix S1, Supporting Information). The 3.23-ha focal area contained a total of 2122 trees with DBH > 7.5 cm (657 trees $ha^{-1}$), 1910 trees with DBH > 10 cm (591 trees $ha^{-1}$), 1773 trees with height > 5 m and DBH > 7.5 cm (549 trees $ha^{-1}$), and 1093 trees with height > 10 m and DBH > 7.5 cm (338 trees $ha^{-1}$). Of all trees with DBH > 7.5 cm, 290 (14%) were dead (and still standing, but in some cases partially broken). All fieldwork was conducted under a research permit issued by the California Department of Parks and Recreation (Sierra District Permit #9-2018 as amended).

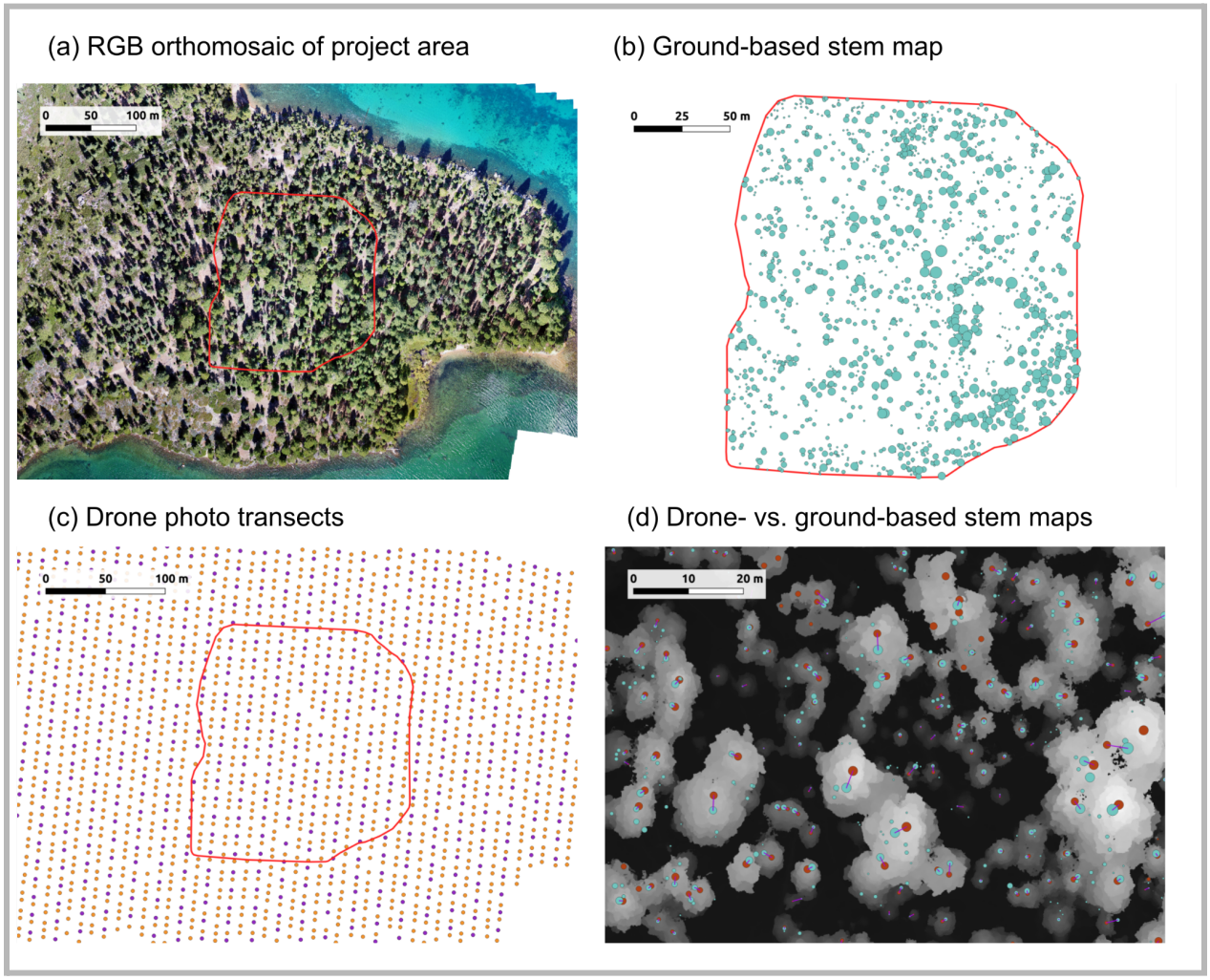

**Fig. 2:** (a) RGB orthomosaic of the project area, with the 3.23-ha focal area indicated with a red outline. (b) The ground-based tree stem map of all trees > 5 m tall constructed as a basis for evaluation of drone-derived stem maps, with larger points indicating taller trees. (c) Spatial locations of drone photos from two drone photo sets ("high nadir" 95% front and side overlap in yellow; and "high nadir" 90% front and side overlap in purple; Table 2). (d) Canopy height model (lighter indicates taller) of a section of the focal area, with ground-mapped trees shown as light blue points, drone-mapped trees shown as dark red points, and pairings between ground- and drone-mapped trees shown as purple lines. In (d), the canopy height model was created by applying photogrammetry parameter set 16 (Table 3) to the "high nadir" photo set with 90% front and side overlap (Table 2). The drone-derived stem map was obtained by applying tree detection algorithm "vwf_059" (Appendix S2: Table S1) to this same canopy height model.

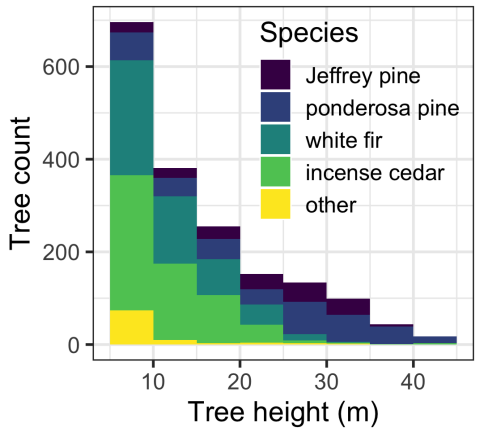


**Fig. 3:** Size class distribution of trees within the 3.23-ha ground-reference stem map.

*Imagery collection and pre-processing*

We collected RGB aerial photographs using a DJI Phantom 4 Advanced quadcopter (SZ DJI Technology Co., Ltd.), which has a 1", 20 megapixel (5472 x 3648 pixel) CMOS sensor, an

8.8 mm focal length, and an 84° diagonal field of view (74° horizontal field of view; 53° vertical field of view). We planned and executed missions using the MapPilot software (Drones Made Easy) on an iPad Pro 9.3" (Apple Inc.) connected to the drone's remote controller. The missions consisted of multiple parallel straight-line transects across the study area (and extending at least 100 m beyond it on all sides) (Fig. 2c), with transect spacing and image spacing along transects set to achieve the specified percentage of overlap between adjacent images (Table 1). We report image overlap percentage for a mission in the format "front overlap/side overlap", with units in percent (e.g., "80/80"). Actual image overlap inevitably differs slightly from the specified overlap (e.g., due to occasionally missed photos, a normal occurrence with some common DJI drones; Fig. 2c), so we treat the overlap amount as a "nominal overlap," reflecting what a future user may expect when using these settings with a similar aircraft. We collected multiple image datasets using different flight parameters (altitude, gimbal pitch, and image overlap) (Table 2). For the missions with 25° camera gimbal pitch (i.e., "oblique", with camera angled 25° up from nadir), we flew two perpendicular sets of transects (N-S and E-W) so that a given point on the landscape would be photographed from four directions. In reporting the percent image overlap of these sets, we report the two missions (N-S and E-W) together in brackets (e.g., "[80/80 + 80/80]"). The overall image density (and mean overlap percent) for two combined 80/80 overlap missions is equivalent to that of a 90/80 or 80/90 overlap mission. For the nadir missions, we only flew N-S transects and only report a single front/side overlap pairing.

All missions used automatic exposure and automatic white balance settings and were flown in MapPilot's "connectionless" mode. We used the "terrain awareness" function so that the aircraft remained at a constant altitude above ground level (as determined by the 30 m Shuttle Radar Topography Mission elevation model; Farr et al., 2007) throughout the mission. Images were collected between 11 am and 3 pm local time (where solar noon was 1:04 pm) on 9-12 September, 2019, by a remote pilot (D. Young) licensed by the United States Federal Aviation Administration (FAA) and following all applicable FAA regulations. During the flights, winds were

light to moderate, visibility was high, and conditions were mostly clear with occasional small clouds for brief periods. We used natural features, with geographic locations identified using Google Earth imagery, as ground control points (Appendix S1, Supporting Information). To test the effect of image overlap on the quality of the resulting tree maps, we subsetted the photo sets to effectively reduce image overlap by retaining every *n*th image on every *n*th transect (Appendix S1, Supporting Information).

**Table 1:** Parameters for image collection flights. Photo set numbers in parentheses are the photo set ID numbers used in the data files and scripts in the repository accompanying this paper.

| Photo set name (ID) | Altitude above ground (m) | Camera gimbal pitch | Transect orientation | Front overlap (%) | Side overlap (%) |
|---|---|---|---|---|---|
| High nadir (14) | 120 | 0° (nadir) | N-S | 95 | 95 |
| Low nadir (15) | 90 | 0° (nadir) | N-S | 95 | 95 |
| High oblique (26) | 120 | 25° (oblique) | N-S | 90 | 90 |
| | | | E-W | 90 | 90 |
| Low oblique (27) | 90 | 25° (oblique) | N-S | 90 | 90 |
| | | | E-W | 90 | 90 |

Finally, we tested whether combining nadir (0°) and oblique (25°) camera pitch missions into a single composite photo set yielded improved photogrammetric performance and ultimately more accurate tree maps. For each flight elevation (90 m and 120 m), we prepared two composite photo sets with different overlaps (Appendix S1). We report the overlap percentages of these composite datasets as the overlap of a pair of oblique missions (in brackets) plus single nadir mission (e.g., [80/80 + 80/80] + 90/80). The overall image density (and thus mean overlap percent) for a [80/80 + 80/80] + 90/80 overlap dataset is nominally equivalent to the image density of a single 90/90 overlap mission.

**Table 2:** The photo set (flight and image overlap) parameters tested to evaluate the effect of flight altitude, camera pitch, and image overlap on quality of the resulting photogrammetry products for tree mapping (Stage 2). The multiple image overlap values were obtained by thinning the originally collected image datasets (Table 1). Overlap pairings in brackets (e.g., [90/90+90/90]) refer to the combination of N-S and E-W missions with oblique camera pitch. Oblique pairings are combined with nadir missions to create composite sets (e.g., [90/90+90/90] + 95/90). The bolded text indicates the two photo sets that were also used in identifying the best Metashape photogrammetry parameter sets (Stage 1).

| Photo set group | Altitude above ground (m) | Camera gimbal pitch | Nominal image overlaps tested (front/side) (%) |
|---|---|---|---|
| **High nadir** | **120** | **0°** | 80/80, 90/80, 80/90, **90/90**, 95/90, 90/95, 95/95 |
| **Low nadir** | **90** | **0°** | 80/80, 90/80, 80/90, **90/90**, 95/90, 90/95, 95/95 |
| High oblique | 120 | 25° | [80/80+80/80], [90/90+90/90] |
| Low oblique | 90 | 25° | [80/80+80/80], [90/90+90/90] |
| High composite | 120 | 0° and 25° | [80/80+80/80] + 90/80, [90/90+90/90] + 95/90 |
| Low composite | 90 | 0° and 25° | [80/80+80/80] + 90/80, [90/90+90/90] + 95/90 |

*Photogrammetric processing and post-processing*

We performed photogrammetric structure-from-motion (SfM) processing of the aerial image sets (see *Introduction*) to produce 3D point clouds and digital surface models using Metashape version 1.6.5 (Agisoft, LLC). We interfaced with Metashape via its Python API using the UC Davis Metashape workflow software version 0.1.0 (Young et al., 2021), which executes a full photogrammetry workflow from end to end using the processing parameters specified in a configuration file by the user. The workflow reads GCP location data from delimited text files prepared in advance.

Our first objective was to determine the combination of photogrammetry processing parameters that maximized the quality of the photogrammetric products for the purpose of tree mapping (Stage 1). We evaluated all factorial combinations of the photo alignment quality parameter (low, medium, or high, corresponding to image upscaling factors of 4, 2, or 1, respectively), the dense cloud quality parameter (medium or high, corresponding to image upscaling factors of 4 or 2, respectively), and the depth filtering intensity parameter (mild or moderate). Upscaling factors refer to the amount by which the image resolution was upscaled (coarsened) in each dimension; for example, with an upscaling factor of 4, the resulting image resolution in x and y dimensions would be ¼ of its original, with each coarse pixel representing the average of 16 original pixels (a 4 x 4 square) (Agisoft, 2020). Recent work has suggested the “medium” and “high” dense cloud quality parameters yield superior ITD results while avoiding extreme computational expense associated with the “very high” parameter; it has similarly shown the “mild” and “moderate” depth filtering parameters to be among those yielding best ITD performance (Tinkham & Swayze, 2021). The three-way factorial combination of photo alignment quality, dense cloud quality, and depth filtering parameters yielded 12 different processing configurations (Table 3), which we ran on two different aerial photo sets: the 120 m nadir (0° camera pitch) mission with 90% front and side photo overlap, and the 90 m nadir mission with 90% front and side photo overlap.

After identifying four Metashape parameter sets that yielded the best tree detection results for these two photo sets (see *Individual tree detection* and *Identification of best-performing methods*, below), we used each of these four parameter sets to process all of the photo sets (Table 2) to enable an evaluation of the effect of of flight altitude, image overlap, and camera pitch on tree mapping performance (Stage 2). Processing all 22 photo sets with the four Metashape parameter sets resulted in running 88 photogrammetry workflows. All processing parameters besides photo alignment quality, dense cloud quality, and depth filtering intensity were held constant across all runs (Appendix S1). These included 100 maximum

neighbors for dense cloud reconstruction, adaptive camera model fitting of all camera model parameters, and default Metashape Python API values for all other parameters. The workflow included a modified, automated version of a sparse point cloud filtering procedure recommended by the USGS (2017) (Appendix S1). In full, the Metashape workflow had the following steps: add photos, align photos, filter sparse cloud points, add GCPs, optimize cameras (using GCPs only), filter sparse cloud points again (based on reprojection accuracy only), build dense cloud, and build digital surface model. The procedure yielded a digital surface model (DSM) and dense point cloud. The code we used to automate this workflow is published (Young et al., 2021).

We normalized and resampled the products of the photogrammetry workflow to obtain, for each run of the workflow, a CHM with 0.12 m resolution (Fig. 2d) and a point cloud with 70 to 100 points $m^{-2}$ (Appendix S1).

**Table 3:** Metashape photogrammetry processing parameter combinations tested (Stage 1). The image upscaling factor (in parentheses) refers to the factor by which image resolution was upscaled (coarsened), in each dimension, prior to processing (photo alignment or dense cloud creation). The four parameter sets that yielded the best tree detection results and were subsequently used in the evaluations of flight altitude, camera pitch, and overlap (Stage 2) are bolded. Parameter set numbering starts at 7 because we preliminarily tested sets with “low” dense cloud quality (upscaling factor of 8; set IDs 1-6) but excluded them from full testing due to poor 3D reconstruction; we retain the original numbering so that it matches the configuration files and analysis code in the repository accompanying this paper.

| Photogrammetry parameter set ID | Photo alignment quality (image upscaling factor) | Dense cloud quality (image upscaling factor) | Depth filtering intensity |
|---|---|---|---|
| 7 | low (4) | medium (4) | mild |
| 8 | low (4) | medium (4) | moderate |

| | | | |
|---|---|---|---|
| **9** | **medium (2)** | **medium (4)** | **mild** |
| 10 | medium (2) | medium (4) | moderate |
| **11** | **high (1)** | **medium (4)** | **mild** |
| 12 | high (1) | medium (4) | moderate |
| 13 | low (4) | high (2) | mild |
| 14 | low (4) | high (2) | moderate |
| **15** | **medium (2)** | **high (2)** | **mild** |
| **16** | **medium (2)** | **high (2)** | **moderate** |
| 17 | high (1) | high (2) | mild |
| 18 | high (1) | high (2) | moderate |

*Individual tree detection (ITD)*

During Stage 1 of methods evaluation (focused on identifying the best Metashape photogrammetry parameters and tree detection algorithms), we tested a wide range of tree detection algorithms. We first tested the “variable window filter” (VWF) algorithm of Popesu and Wynne (2004) as implemented in the R package ForestTools version 0.2.1 (Plowright, 2021). This function uses the CHM raster and evaluates each pixel as a potential tree top by searching all pixels within a particular radius around the focal pixel and labeling the focal pixel as a tree top if it has the maximum height value with the search radius. The search radius is determined by a linear function of the height of the focal pixel. We tested 76 different combinations of the intercept and slope parameters of this linear function (Appendix S2: Table S1). For each of these parameter sets, we also tested three different CHM smoothing options. These smoothing functions were implemented as moving window algorithms which, for each pixel, computed the mean of all pixels in a *n* x *n* pixel square centered around the focal pixel and assigned the resulting value to the focal pixel. We tested a 5 x 5 pixel window (0.6 x 0.6 m; Smooth: 1), a 9 x 9 pixel window (1.08 x 1.08 m; Smooth: 2), and no smooth (Smooth: 0). The smooths were applied prior to running the VWF algorithm. We included these smoothing options with the

thought that they may smooth over 3D reconstruction artifacts of the photogrammetry algorithm. Factorially combining the three smooth options with each of the 76 variable window filter parameter sets resulted in testing 228 implementations of the VWF-based tree detection algorithm (Appendix S2: Table S1).

We additionally tested six algorithms designed to identify trees directly from 3D point clouds, implemented in the R packages lidR v3.0.4 (Roussel, 2021a) and lidRplugins v0.2.0 (Roussel, 2021b) (Appendix S2: Table S2). Most of these algorithms accept one or more parameters; we tested a variety of parameter combinations, focusing on those that Koontz et al. (2021) found to produce the best tree detection results. Two of the algorithms ('hamraz' and 'layerstacking'; Appendix S2: Table S2) were not tested by Koontz et al. The 'hamraz' algorithm requires no parameters and 'layerstacking' requires a single binary parameter for "hardwood" or "conifer"; we tested both. Additionally, for each point cloud-based algorithm, we tested the effect of thinning ("decimating") the point cloud to 50 or 10 points $m^{-2}$ prior to running each algorithm. The multiple parameter combinations tested across all the point cloud-based tree detection methods resulted in a total of 58 methods tested. Combined with the CHM-based VWF methods, we tested a total of 286 tree detection methods for each of the 12 Metashape photogrammetry workflows (Table 3) that were run for the Stage 1 comparisons. For the Stage 2 comparisons, we used four top-performing tree detection methods (see *ITD performance evaluation*).

*ITD performance evaluation*

We quantified the accuracy of the drone-derived tree maps by comparing each one against the 3.23-ha ground-based stem map. An initial coarse filter was applied to eliminate the very poor quality drone-derived maps: if the number of drone-mapped trees > 10 m height was more than 5 times the number of ground-mapped trees > 10 m height, or if it was less than 1/10

the number of ground-mapped trees > 10 m height, it was eliminated from the pool of candidates.

For all remaining drone-derived maps, we programmatically performed a comparison to the ground-derived map on a tree-by-tree basis, determining whether each ground-mapped tree was present in the drone-based map (true positives) and whether there were any additional trees in the drone-derived map that were not present in the ground-derived map (false positives). This required determining which tree (if any) from the ground-based map corresponded to which tree in the drone-based map (and vice-versa), a challenging and subjective exercise given that we never expect trees in a ground-based map to perfectly coincide with those in a drone-based map. Differences can arise due to spatial errors in both mapping techniques and also due to the fact that the tree top (the point identified in the drone-based map) is often not located precisely above the stem (the point identified in the ground-based map).

For a drone-mapped tree to match with a ground-mapped tree, it was required to be within a distance ($d_{max}$) of the ground-mapped tree defined as a function of the height ($h$) of the ground-mapped tree as

$$d_{max} = 0.1h + 1,$$

where units are in meters. Its height was also required to be within ± 50% of the height of the ground-mapped tree. Thus, for a ground-mapped tree 10 m tall, a drone-mapped tree needed to be within 2 m distance and its height needed to be between 5 and 15 m to match. For a ground-mapped tree 30 m tall, a drone-mapped tree needed to be within 4 m distance and its height between 15 and 45 m. Our distance matching threshold was generally similar to or more conservative than that used by previous studies (e.g., 4 m used by Swayze et al., 2021 and 3 m used by Creasy et al., 2021). We used a more liberal height range for tree matching than previous studies (e.g., ± 10% used by Creasy et al., 2021 and ± 2 m used by Swayze et al., 2021) because (a) we wanted to avoid artificially reducing the estimated error in drone-based

tree height measurement (as error estimation relies on comparing heights of drone-detected trees vs. paired ground-mapped trees) and (b) error substantially less than the matching threshold in drone- vs. ground-mapped height would provide evidence that trees were correctly matched.

For each ground tree, the nearest matching drone tree was assigned as its match. If the same drone tree was assigned to multiple ground trees, it was removed from all of the ground trees except the one spatially closest to it. This procedure was repeated two more times, each time for the ground and drone trees remaining (unmatched) following the previous iteration. After the third iteration, no further matches were possible.

To quantify individual tree detection (ITD) accuracy, we computed the true-positive rate ("sensitivity" or "recall", the proportion of ground-mapped trees that had a matching drone-mapped tree) and the precision (the proportion of drone-mapped trees that matched a ground-mapped tree). Because it is possible for a tree detection algorithm to achieve high sensitivity at the expense of precision (and vice-versa), we also computed the F score, which integrates sensitivity and precision by computing their harmonic mean, thus disproportionately penalizing low values and favoring balanced sensitivity and precision. We computed sensitivity, precision, and F score for two different tree size groups: trees ≥ 10 m height, and trees ≥ 20 m height.

There is potential for edge effects to confound the tree detection accuracy inferred via tree matching. If a ground-mapped tree were just inside the analysis boundary and the corresponding drone-mapped tree just outside it, the ground-mapped tree would be considered to not have a match (and thus constitute a false-negative detection). To minimize this effect, when calculating the proportion of drone-mapped trees that matched ground-mapped trees, we considered only drone-mapped trees that were at least 5 m inside the project boundary (so that they all had an opportunity to be matched with ground-mapped trees in any direction). We did

the same with ground-mapped trees when calculating the proportion of ground-mapped trees that matched drone-mapped trees.

While it is valuable to know the proportion of all ground reference trees that can be detected from aerial imagery, it is unrealistic to expect all trees to be detected, particularly in structurally complex stands like ours where small trees may be hidden under large trees or two immediately adjacent trees of similar size appear as one. Therefore, in addition to evaluating ITD performance across all trees, we evaluated performance in mapping “dominant” trees that did not have any immediately adjacent taller neighbors (Appendix S1).

*Identification of best performing methods*

To identify the best performing photogrammetry and tree-detection parameter sets (Stage 1), we first identified the photogrammetry parameter sets that most consistently yielded the highest F score (or within 0.005 of the highest F score) across all factorial combinations of photogrammetry parameter set (7-18; Table 3), photo set (High nadir 90/90, Low nadir 90/90; Table 2), tree height class (> 10 m or > 20 m), and tree position class (all trees or dominant trees only). When evaluating the F score for a given combination of photogrammetry parameterization, flight altitude, tree height class, and tree position class, we used the F score from the tree detection parameterization with the highest F score across all 286 parameterizations tested; this parameterization could be different for each combination. We selected four photogrammetry parameter sets. Using only those four sets, we then selected the tree detection parameter sets that most consistently yielded the highest F score (or within 0.005 of the hightest F score) across all factorial combinations of photogrammetry parameter set, flight altitude, tree height class, and tree position class (Appendix S2: Table S4). We selected 8 tree detection parameter sets.

To quantify the influence of flight altitude, image overlap, and camera pitch on ITD performance (Stage 2), we used the four best-performing photogrammetry parameter sets,

combined factorially with the eight best-performing tree detection methods, to produce 32 tree maps from each of the 22 different photo sets (Table 2). When plotting or describing tree detection performance achieved with any of these photo sets, we report the F score obtained from the tree detection method that produced the maximum F score for that photoset.

*Evaluation of drone-based tree height measurement*

To evaluate the potential to measure tree heights using drone imagery, we extracted tree heights from the canopy height model produced by using photogrammetry parameter set 16 (Table 4) on the high (120 m) nadir photo set with 90% front and side image overlap. We used this CHM because it was among the best-performing for individual tree detection (see Results). We extracted the height value from the CHM pixel beneath each detected treetop. We then compared these extracted heights to the ground-measured heights of the ground reference trees to which the drone-detected trees were paired (see *ITD performance evaluation*). Ground reference trees that were not paired with drone-detected trees, and vice versa, were not included in the comparison.

**Results**

*Stage 1: Optimal photogrammetry and tree detection parameters*

Photogrammetry parameter combination 16 (medium alignment quality, high dense cloud quality, moderate depth filtering) consistently enabled the most accurate tree detection performance as quantified by F score (Fig. 4 and Appendix S2: Table S3), though the differences among parameter combinations were relatively small ($\Delta F < 0.04$). Medium alignment quality and high dense cloud quality both involve upscaling (coarsening) the image by a factor of 2 in both dimensions prior to running the algorithm. Parameter set 16 achieved the highest (or within 0.005 of the highest) F scores across all factorial combinations of flight altitude (90 m or 120 m), tree position (all trees or dominant trees), and tree height class (> 10 m or > 20 m).

Therefore, for further evaluation, we focused on parameter set 16, along with parameter sets 9, 11, and 15, which were among the best-performing parameter sets for multiple combinations of tree height, tree position, and flight altitude (Appendix S2: Table S3). We thus selected a total of four photogrammetry parameter sets for further evaluation.

The most accurate tree detection methods, as quantified by F score, were all CHM-based VWF methods (Appendix S2: Table S4). This was true across all factorial combinations of flight altitude (90 m or 120 m), tree height class (> 10 m or > 20 m), tree position (all trees or dominant trees), and photogrammetry parameters (sets 9, 11, 15, and 16). Across all of these combinations, methods vwf_121 and vwf_196 most consistently achieved the highest (or within 0.005 of the highest) F scores for tree detection accuracy (Appendix S2: Table S4). Therefore, for further evaluation, we focused on these methods, along with six other consistently top-performing methods, vwf_109, vwf_110, vwf_113, vwf_120, vwf_122, vwf_185, for a total of 8 tree detection methods. Among the point cloud-based methods, parameterizations of the method of Li et al. (2012) generally performed the best. For the 120 m nadir photo set with 90% front and side overlap processed using photogrammetry parameter set 16, the F score for the Li et al. (2012) method was 0.04 to 0.06 less than the F score of the top-performing VWF parameterization, depending on the tree height class and canopy position (Appendix S2: Table S5).

For a given scenario (e.g., flight altitude, tree position, tree height, camera pitch, and photo overlap), the F score achieved by the combination of photogrammetry parameter set 16 and tree detection method vwf_196 was generally within 0.01 of the maximum F score achieved by the optimal combination of photogrammetry parameter set (out of the four best-performing options) and tree detection method (out of the eight best-performing options) (e.g., Table 4). The difference in F score was less than 0.01 in approximately 80% of scenarios, particularly those with at least 90% front and side photo overlap and nadir images (Appendix S2: Table S6). In photo sets with less overlap and/or oblique images, other photogrammetry and tree detection

parameters often performed better (F score difference > 0.01), but for these scenarios, even the optimal photogrammetry and tree detection parameter combinations yielded inferior tree mapping performance relative to higher overlap and/or nadir imagery (see *Stage 2: Optimal image collection parameters*).

For nadir photo sets with at least 90% front and side overlap, the optimal combination of photogrammetry and tree detection parameters achieved tree mapping accuracy ranging between F = 0.67 and F = 0.87 (Appendix S2: Table S6). For example, for dominant trees > 10 m tall, the optimal methods (photogrammetry parameter set 16 paired with tree detection method vwf_196, applied to the 90% front and side overlap 120 m nadir mission) achieved an F score of 0.78, with a sensitivity of 0.69 and a precision of 0.90 (Table 4). Generally, precision was greater than sensitivity (Table 4 and Appendix S2: Table S6).

**Table 4:** Tree mapping accuracy achieved with the optimal combination of photogrammetry parameter set and tree detection method (Category 1) or with the specific combination of photogrammetry parameter set 16 and tree detection method vwf_196 (Category 2) for each factorial combination of tree position (dominant or all) and tree height class (> 20 m or > 10 m). All scenarios use the high (120 m altitude) nadir photo set with 90% front and side overlap. For two scenarios (dominant trees > 10 m and all trees > 20 m), the combination of photogrammetry parameter set 16 and tree detection method vwf_196 is the optimal combination. For accuracy metrics for different flight altitudes, camera pitches, and photo overlaps, see Appendix S2: Table S6.

| | | Category 1: Photogrammetry and tree detection parameter sets yielding maximum F | | | | | Category 2: Photogrammetry parameter set 16 and tree detection method vwf_196 | | |
|---|---|---|---|---|---|---|---|---|---|
| Canopy position | Tree height | Photogrammetry parameter set | Tree detection method | F score | Sensitivity | Precision | F score | Sensitivity | Precision |
| dominant | > 20 m | 11 | vwf_122 | 0.865 | 0.838 | 0.894 | 0.864 | 0.841 | 0.887 |
| dominant | > 10 m | 16 | vwf_196 | 0.783 | 0.691 | 0.903 | 0.783 | 0.691 | 0.903 |
| all | > 20 m | 16 | vwf_196 | 0.826 | 0.756 | 0.909 | 0.826 | 0.756 | 0.909 |
| all | > 10 m | 15 | vwf_121 | 0.672 | 0.571 | 0.814 | 0.665 | 0.519 | 0.924 |

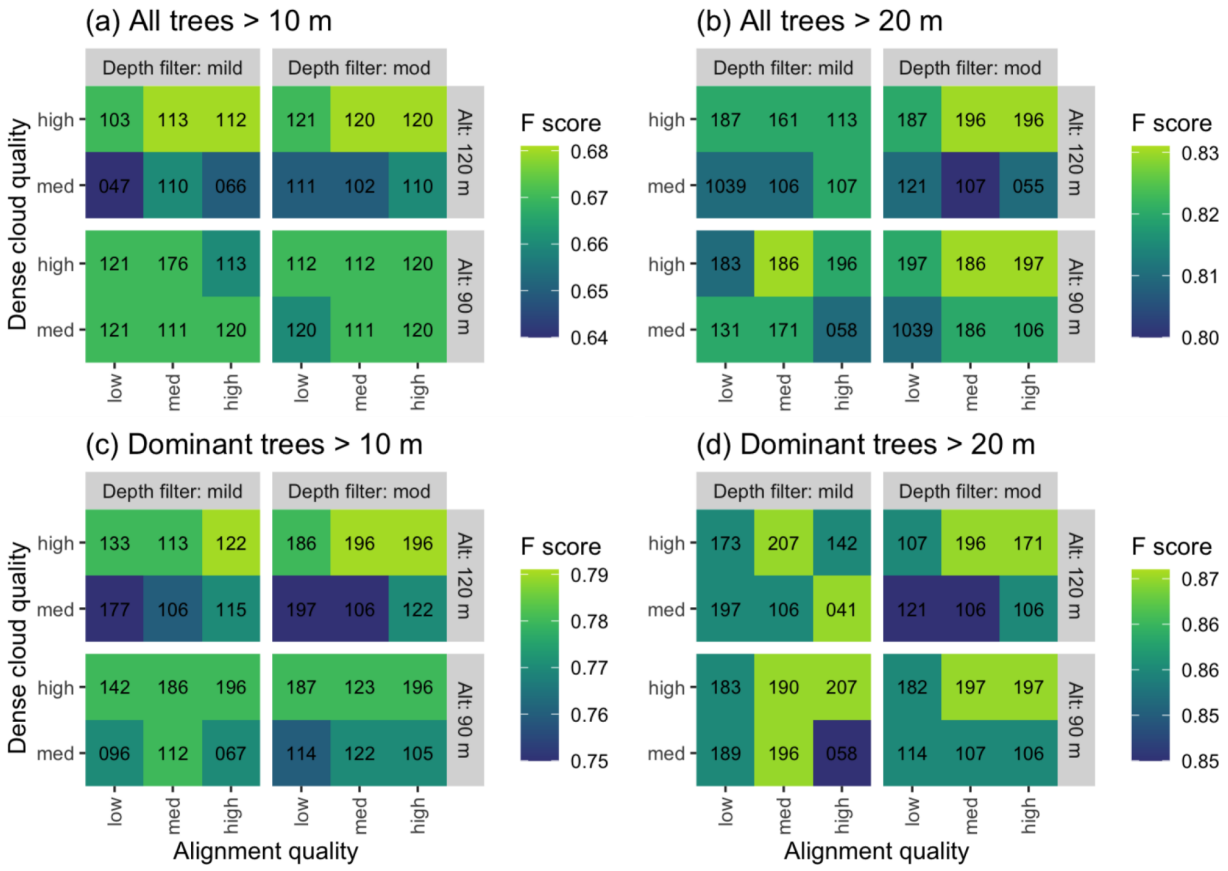


**Fig. 4:** Individual tree detection performance of different photogrammetry parameter combinations at two flight altitudes, for all trees (a, b) and dominant trees (c,d) with height > 10 m (a, c) or height > 20 m (b, d). The number in each cell indicates the ID of the tree detection method (Appendix S2: Tables S1-S2) that yielded the maximum F score for the particular combination of parameters; 3-digit numbers refer to VWF methods, while 4-digit numbers refer to point cloud-based methods. The F score itself is indicated by the color. The aerial photo sets processed were the high nadir set (Alt: 120 m) and the low nadir set (Alt: 90 m) (both with 90% front and side image overlap) (bolded entries in Table 2).

*Stage 2: Optimal image collection parameters*

Tree mapping accuracy tended to increase with increasing image overlap, to a point: once overlap percent reached 90/80 (front/side), additional increase in overlap (to 90/90 or greater) yielded little increase in accuracy (Fig. 5). At 90/90 percent overlap, both 120 m and 90 m nadir flights yielded F scores of about 0.78 for dominant trees > 10 m tall and about 0.86 for dominant trees > 20 m tall (Appendix S2: Table S6). Among nadir image sets, higher-altitude (120 m) sets tended to yield greater accuracy than lower-altitude sets when image overlaps were lower (below 90/90) and similar accuracy when overlaps were greater (90/90 and greater) (Fig. 5). Interestingly, even though the 90/80 and 80/90 percent overlap image sets contained roughly the same image density, the former consistently enabled substantially greater tree mapping accuracy, for both 120 m and 90 m flights (Fig. 5).

Nadir imagery tended to achieve accuracy greater than or comparable to that of oblique or nadir-oblique composite imagery of similar image density (Fig. 5). The 120 m composite nadir-oblique image set performed as well as (at higher overlap) or substantially better than (at lower overlap) the 90 m composite pitch image set. For a similar image density (i.e., mean overlap), a 120 m nadir flight (at, e.g., 90/80 percent overlap) yielded similar accuracy as the combined N-S and E-W oblique flights (at, e.g., [80/80 + 80/80] overlap).

All of the results presented thus far in this section assume that a given image set is processed using the photogrammetry and tree detection parameters that yield the greatest accuracy for that set. When using a single top-performing photogrammetry parameter set (16) combined with a single top-performing tree detection method (vwf_196), the patterns remain qualitatively very similar, with generally only very small shifts in tree detection accuracy (Appendix S1: Fig. S2).

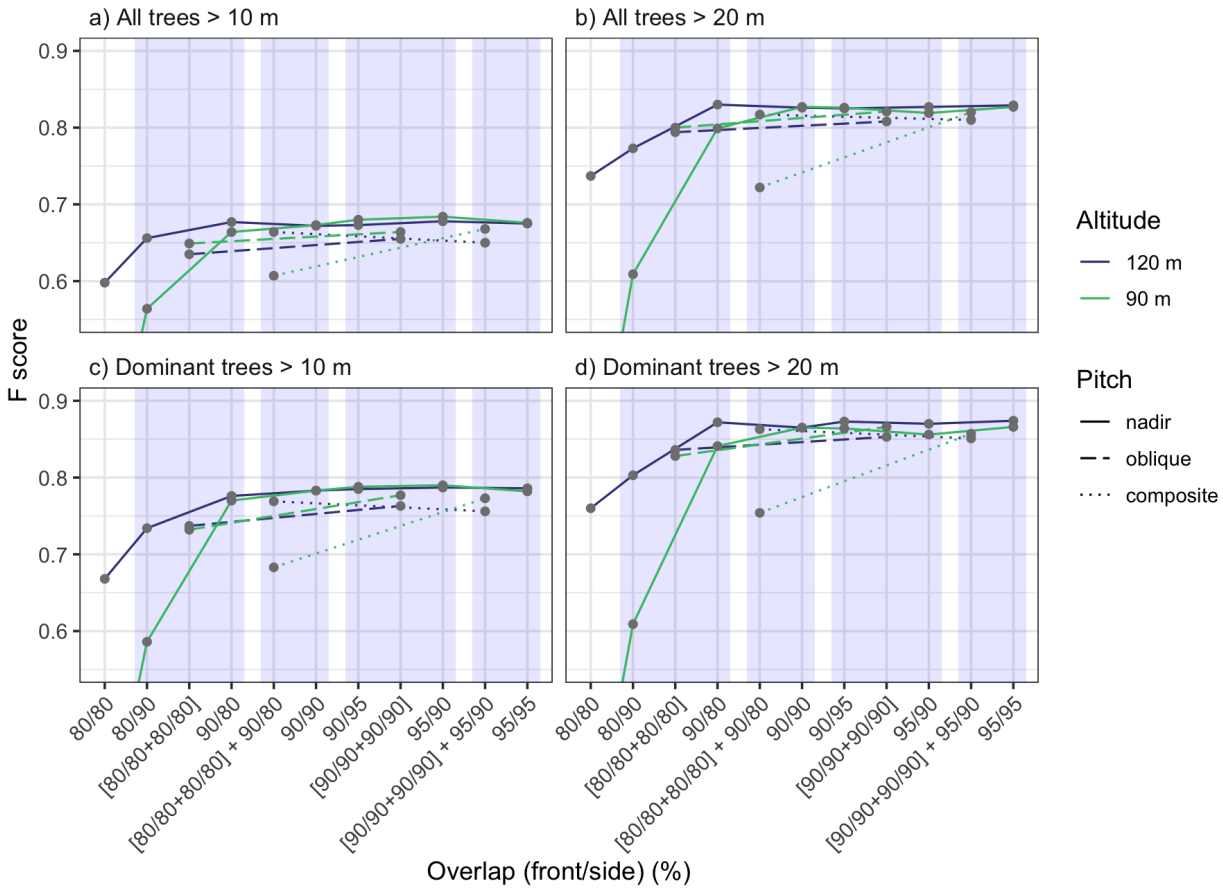


**Fig. 5:** Individual tree detection F score for different flight altitude, camera pitch, and image overlap combinations. For each combination, 8 top-performing tree detection methods were combined factorially with 4 top-performing photogrammetry processing parameter sets (see Fig. 1), and the F score depicted is the maximum across these 32 combinations. From left to right, the x-axis represents categories of image overlap with a monotonic, but not consistent, increase in nominal image density. All overlap values within vertical blue shaded regions correspond to the same nominal image density. Points are connected by lines simply for ease of associating altitude and pitch with points. Overlap pairings in brackets (e.g., [90/90+90/90]) refer to the combination of N-S and E-W missions with oblique camera pitch. Oblique pairings are combined with nadir missions to create composite pitch sets (e.g., [90/90+90/90] + 95/90). For a version of this figure that uses only the single consistently best-performing tree detection method (vwf_196)

combined with the best-performing photogrammetry parameter set (16), see Fig. S2 (Appendix S1).

*Tree height measurement*

Tree height measurement was generally highly accurate, with drone-measured and ground-measured tree heights corresponding with $R^2$ = 0.95, a mean bias of -0.86 m (with drone-derived heights generally shorter than their ground reference counterparts), and a mean absolute error of 1.82 m (Fig. 6). The mean absolute error as a percentage of each tree's height was 9% and the mean bias was -3%.

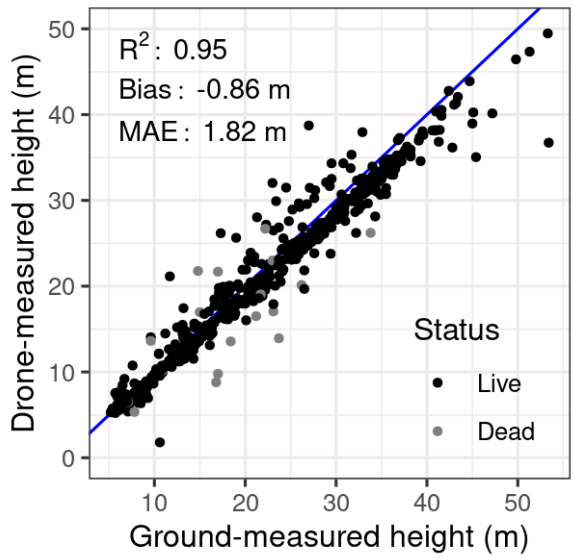


**Fig. 6:** Drone-based tree height measurements (height value of the CHM at each treetop location) relative to ground reference tree heights for the most consistently best-performing tree detection method (vwf_196) applied to the CHM produced using the most consistently high-performing photogrammetry parameter combination (16) on the high (120 m) nadir 90% front and side overlap photo set. The blue line is the 1:1 line.

## Discussion

*Imagery acquisition and processing*

Our work helps to identify top-performing approaches to imagery collection and processing for SfM-based forest mapping in structurally complex conifer forests using relatively low-cost RGB drones. Several clear and consistent results can help forest scientists and managers efficiently produce high-quality forest maps. First, a high flight altitude (120 m, the maximum flight altitude generally allowed by the FAA) consistently yielded tree maps with accuracy better than or effectively equivalent to those obtained from lower altitude (90 m) flights (Fig. 5), consistent with previous observations that flight altitude has minimal impact (Swayze et al., 2021; Torres-Sánchez et al., 2018). Even in contexts where stem map quality is insensitive to flight altitude (in our case, when image overlap is 90% or greater), 120 m flights will likely be preferred given that they require fewer images to cover a landscape (as each image encompasses more ground area) and therefore less flight time.

Similarly, our work reveals little if any gain in ITD accuracy by increasing image overlap above 90% (front and side) (Fig. 5), consistent with previous results showing decreasing marginal returns to ITD accuracy with increasingly high overlap (Torres-Sánchez et al., 2018). In fact, given that increasing image overlap can substantially increase flight time (e.g., increasing side overlap from 90% to 95% doubles the number of transects, thus doubling flight time), flights with overlap > 90% may be undesirable. Reducing side overlap to 80% (while keeping front overlap at 90%) resulted in only minimal change in ITD accuracy. Therefore, given flight time constraints or the need to cover extensive area, 90/80 front/side overlap percent may be preferable. Surprisingly, photo sets with 90/80 front/side overlap consistently yielded ITD accuracy substantially greater than that from sets with 80/90 front/side overlap (Fig. 5), despite the fact that the image density of these two sets is nominally identical. This asymmetry may be a consequence of the default “generic” image pair preselection (initial image matching) algorithm used by Metashape, which initially attempts to pair images chronologically; greater overlap

along the forward image dimension may facilitate this critical initial step. Alternatively or in addition, greater overlap along the shorter dimension of the image may disproportionately facilitate image matching and/or depth mapping, as it makes the overlap portion more square (as opposed to a thin strip that may lack sufficient spatial context).

Our tests of camera pitch revealed that oblique (25°) and oblique-nadir composite imagery, regardless of flight altitude, yielded ITD accuracy worse than nadir imagery collected at 120 m. This finding is surprising because oblique imagery is known to yield more accurate terrain models (Nesbit & Hugenholtz, 2019) and increase understory point cloud density (Díaz et al., 2020), especially in stands without a closed canopy (Lamping et al., 2021). However, our findings corroborate existing evidence that for ITD specifically, greater accuracy is achieved with nadir imagery (Swayze et al., 2021). Although the improved understory imaging that is achieved by using oblique imagery can improve estimates of tree DBH (by enabling more accurate 3D modeling of tree stems; Swayze et al., 2021), it apparently does not improve the potential for detection of understory trees. This limitation to improvement may be explained by the fact that all CHM-based tree detection algorithms and many point cloud-based tree detection algorithms (e.g., Li et al., 2012) are not designed to detect one tree beneath another, so improved imaging of the understory cannot translate to improved tree detection. Improvements to multi-layer tree detection algorithms (e.g., Torresan et al., 2020; Xiao et al., 2019), and implementations of them in common point cloud processing platforms (e.g., the R package lidR; Roussel, 2021a), may make understory imaging (and thus oblique camera angles) more valuable for ITD in the future.

We expect our results are applicable to many widely used, relatively low-cost drones with an RGB camera that has a resolution and field of view similar to ours. In fact, given that all image processing steps in the optimal parameterization utilize images that have been upscaled (coarsened) twofold in both dimensions (thus converting a 20 megapixel image to 5 megapixels), the same dataset could in theory be generated with a 5 megapixel camera by eliminating the upscaling step, assuming optical quality is otherwise similar. Similarly, imagery

from a higher-resolution camera could be used optimally by increasing the upscaling factor. While this may represent a waste of data, the coarser scale may actually achieve greater mapping accuracy given that tree canopies largely consist of small surfaces (e.g., leaves, branches) that can move in the wind and thus confound the image-matching algorithms central to the photogrammetry software.

*Tree detection algorithms*

Despite testing 6 point cloud-based ITD algorithms (and 58 different parameterizations of them), the CHM-based VWF algorithm consistently performed the best (Appendix S2: Tables S4 and S5), potentially a consequence of the fact that the point cloud-based methods we tested are not designed to detect one tree beneath another and therefore provide little additional fidelity relative to a CHM (see Discussion section *Imagery acquisition and processing*).

As with other SfM-based work (e.g., Creasy et al., 2021; Tinkham & Swayze, 2021) and lidar-based work (Ferraz et al., 2012; Jeronimo et al., 2018), we observed substantially improved ITD performance for taller trees and canopy-dominant trees vs. all trees (e.g., F = 0.78 for canopy-dominant trees > 10 m height vs. F = 0.67 for all trees > 10 m height). This pattern makes sense considering structure can only be mapped for surfaces that are detected by the sensor (which are disproportionately the top-of-canopy objects, especially for SfM; Jayathunga et al., 2018; Lisein et al., 2013). Even when using lidar, which can penetrate tree canopies to some extent, understory and mid-story detail (and thus potential to detect trees there) can be limited, especially when the overstory is dense and/or tall (Campbell et al., 2018). This limitation has led some to re-focus detection and mapping of individual trees (ITD) toward detection and mapping of tree-approximate objects (TAOs), which can include single trees and clusters of trees that are not differentiable (Jeronimo et al., 2018; North et al., 2017). Maps of the size and arrangement of TAOs may be valuable for some management applications (Jeronimo et al., 2018; North et al., 2017), and important ecological questions can be addressed using maps of

the specific trees visible from above (Brandt et al., 2020; Weinstein et al., 2021) or detectable using SfM that is not canopy-penetrating (Koontz et al., 2021). Our calculation of ITD accuracy metrics specifically for “overstory” trees helps to provide a sense of TAO mapping accuracy. Given that we used a conservative set of parameters for classifying a tree as “canopy dominant” (Appendix S1: Fig. S1), our accuracy metrics may be underestimates.

Notably, our ITD precision values were consistently higher than the sensitivity values, especially for all trees (as opposed to canopy-dominant trees) (Table 4 and Appendix S2: Table S6), indicating that the ITD algorithm failed to detect some trees as a consequence of minimizing false-positives. This suggests that there is some potential to select an ITD parameterization with greater tree detection sensitivity. This may increase the false-positive rate (resulting in an overall lower F score), but future work may incorporate an additional “detected tree screening” stage that uses information besides the CHM or point cloud to identify and reject false positives. For example, Bonnet et al. (2017) used a machine learning approach to predict tree detections as true or false positives based on the textural and spectral characteristics of the detected objects and thereby reduced the false-positive rate from 75-82% to 3-8%. Incorporating both structural and spectral data (e.g., taking advantage of the fact that points in SfM-derived point clouds, in contrast to lidar-derived clouds, can be assigned spectral values) in tree detection algorithms may improve tree detection sensitivity (Yancho et al., 2019).

*Tree height measurement and matching of ground and drone trees*

The canopy height model resulting from the optimal photogrammetry parameter set provided a relatively accurate representation of tree heights (Fig. 6). The small negative height bias (CHM heights < field-measured heights) generally increased with increasing tree height, suggesting either (a) disproportionate overestimation of tall tree heights during ground surveys or (b) disproportionate underestimation of tall tree heights by the photogrammetry algorithm. Given that CHM generation involves some degree of interpolation and smoothing of the point

cloud, it may make sense that objects that are disproportionately tall relative to their surroundings are underestimated by the CHM. Nonetheless, the mean absolute height error was relatively small (1.8 m or 9% of tree height). Further, given that our algorithm for matching SfM-detected trees with ground-measured trees required the SfM tree to be within ± 50% of the height of the ground tree, the fact that the mean height difference was only 9% strongly suggests that trees were generally matched correctly. Our SfM-based tree height measurement accuracy was generally comparable to or better than other SfM-based approaches, which have obtained $R^2$ = 0.71 (Belmonte et al., 2020), RMSE = 9-15% (Creasy et al., 2021), RMSE = 24% (Tinkham & Swayze, 2021), $R^2$ = 0.99 with RMSE = 18% (Swayze et al., 2021), and $R^2$ = 0.94 with RMSE = 12.6% for live trees (Koontz et al., 2021).

*Conclusions*

Our comprehensive evaluation of numerous SfM imagery collection, imagery processing, and tree detection methods led to ITD performance that meets or exceeds expectations based on previous work (Table 5). The majority of SfM-based ITD work to date has been conducted in relatively low density monodominant stands with low structural complexity, and our work demonstrates that SfM-based ITD can also be a practical approach to tree mapping in denser, more structurally complex stands, especially if the focus is on canopy-dominant trees or TAOs. To evaluate the extent to which the ITD accuracy and optimal parameter sets we identified may extend to other forest stands, perhaps the most important considerations are stand density and structural complexity (Jeronimo et al., 2018). In forests with lower tree density and limited multi-stratum structure, such as many ponderosa pine-dominated forests of the southwestern U.S. (e.g., Swayze et al. 2021), we might expect higher accuracy than we achieved; we might expect the reverse for denser or more structurally complex stands. Historical densities of trees with DBH > 10 cm in the yellow pine and mixed-conifer forests of California's Sierra Nevada averaged roughly 195 trees $ha^{-1}$ (Safford & Stevens, 2017; Young et al., 2020), relative to the

591 trees $ha^{-1}$ in our mixed-conifer stand. Considering contemporary stands are roughly 2-4-fold denser than the historical average (Safford & Stevens, 2017) (therefore, roughly 400-800 trees $ha^{-1}$), our focal stand may be roughly reflective of mean contemporary California mixed-conifer forest structure and thus of expected ITD performance. In denser stands with strong multi-stratum structure, the use of oblique images, coupled with a point-cloud based ITD algorithm, will likely become more important for capturing understory trees (see Discussion section *Imagery acquisition*). With additional refinements (e.g., use of a more sensitive tree detection algorithm with a false-positive filtering step, improvement of point cloud-based multi-layer tree detection algorithms, and application of deep learning computer vision to tree detection; Weinstein et al., 2020, 2021), the accuracy and applicability of drone-based forest mapping will continue to improve.

**Table 5.** Summary of recent forest ITD studies that compare drone-derived tree detections to ground reference trees in conifer-dominated forests and assess ITD accuracy using the F score. Note that Koontz et al. (2021) is included here despite not reporting an F score because of the strong similarities in forest structure/type to this study.

| Reference | Overall forest density (trees $ha^{-1}$) | Relative structural complexity | Stratum | F score |
|---|---|---|---|---|
| This study[1] | 549; tree height > 5 m and DBH > 7.5 cm | High | Dominant (no nearby, taller neighbors) | 0.78-0.87 |
| | | | All | 0.67-0.83 |
| Belmonte et al. (2020)[2] | 59; tree height > 1.37 m | Low | All | 0.94 |
| | 139; tree height > 1.37 m | Low | All | 0.8 |
| | 778; tree height > 1.37 m | Low | All | 0.44 |
| Tinkham and Swayze (2021) | 374; tree height > 5 m | Low | Overstory; trees >7m tall | 0.72 |
| | | | Understory; trees <7m tall | 0.6 |
| Swayze et al. (2021) | 374; tree height > 5 m | Low | All | 0.77 |
| Creasy et al. (2021) [KNF site][3] | 504; tree height > 1.37 m | High | All | 0.57 |
| | | | Overstory; trees >20m tall | 0.71 |
| | | | Intermediate; trees between 8 and 20m | 0.57 |
| | | | Understory; trees <8m | 0.51 |
| Creasy et al. (2021) [MEF site][3] | 600; tree height > 1.37 m | Low | All | 0.58 |
| | | | Overstory; trees >18m tall | 0.75 |
| | | | Intermediate; trees between 6 and 18m | 0.53 |
| | | | Understory; trees <6m | 0.50 |
| Koontz et al. (2021)[4] | 537; tree DBH > 6.35 cm | High | All | – |

[1] Range of F scores reflects multiple assessments for trees meeting different height thresholds
[2] Assessment of ITD performed in post-treatment forested landscape with treatment prescription designed to reduce small tree density
[3] F scores reflect best assessment across ITD algorithms; density calculated using total number of trees within 4.5 ha unit
[4] F score not reported; RMSE for drone-derived tree count at plot scale: 46%; Density range: 153-1038 trees $ha^{-1}$

**Acknowledgments**

Our Emerald Point study site is part of the ancestral lands of the Washoe people. We thank data technicians H. de la Calle and S. Sundaram for their careful organization of the drone imagery, identification of ground control points, and preparation of the ground reference stem map data. We thank A. Barker and R. Cuevas for assisting with ground reference stem map data collection and D. Shaw for facilitating field logistics. We thank A. Latimer for assistance acquiring drone equipment and computing resources. We thank A. Mandel and other contributors to the reproducible photogrammetry workflow software library we used. Funding for this project was provided by the California Department of Forestry and Fire Protection's Forest Health Program as part of the California Climate Investments Program (to DJNY) and by Earth Lab through CU Boulder's Grand Challenge Initiative and the Cooperative Institute for Research in Environmental Sciences (CIRES) at CU Boulder (to MJK).

**Author contributions:** DJNY and MJK conceived the ideas and designed the methodology; DJNY and JW collected the data; DJNY analysed the data; DJNY led the writing of the manuscript. All authors contributed critically to the drafts and gave final approval for publication.

**Potential perceived conflicts of interest:** DJNY is employed by both the University of California, Davis, and Vibrant Planet, PBC. The other authors do not declare any potential real or perceived conflicts of interest.

**Data availability:** The raw and processed data and code supporting this publication are available via the Open Science Framework (https://osf.io/kb3nj/; DOI: 10.17605/OSF.IO/KB3NJ; Young et al., 2021).

**Literature cited**


Agisoft. (2020). *Metashape v1.6 downscale parameter*. https://www.agisoft.com/forum/index.php?topic=11697.0

Belmonte, A., Sankey, T., Biederman, J. A., Bradford, J., Goetz, S. J., Kolb, T., & Woolley, T. (2020). UAV-derived estimates of forest structure to inform ponderosa pine forest restoration. *Remote Sensing in Ecology and Conservation*, *6*(2), 181–197. https://doi.org/10.1002/rse2.137

Bonnet, S., Lisein, J., & Lejeune, P. (2017). Comparison of UAS photogrammetric products for tree detection and characterization of coniferous stands. *International Journal of Remote Sensing*, *38*(19), 5310–5337. https://doi.org/10.1080/01431161.2017.1338839

Brandt, M., Tucker, C. J., Kariryaa, A., Rasmussen, K., Abel, C., Small, J., Chave, J., Rasmussen, L. V., Hiernaux, P., Diouf, A. A., Kergoat, L., Mertz, O., Igel, C., Gieseke, F., Schöning, J., Li, S., Melocik, K., Meyer, J., Sinno, S., … Fensholt, R. (2020). An unexpectedly large count of trees in the West African Sahara and Sahel. *Nature*, 1–5. https://doi.org/10.1038/s41586-020-2824-5

Camarretta, N., Harrison, P. A., Bailey, T., Potts, B., Lucieer, A., Davidson, N., & Hunt, M. (2020). Monitoring forest structure to guide adaptive management of forest restoration: A review of remote sensing approaches. *New Forests*, *51*(4), 573–596. https://doi.org/10.1007/s11056-019-09754-5

Campbell, M. J., Dennison, P. E., Hudak, A. T., Parham, L. M., & Butler, B. W. (2018). Quantifying understory vegetation density using small-footprint airborne lidar. *Remote Sensing of Environment*, *215*, 330–342. https://doi.org/10.1016/j.rse.2018.06.023

Creasy, M. B., Tinkham, W. T., Hoffman, C. M., & Vogeler, J. C. (2021). Potential for Individual Tree Monitoring in Ponderosa Pine-Dominated Forests Using Unmanned Aerial System Structure from Motion Point Clouds. *Canadian Journal of Forest Research*, cjfr-2020-0433. https://doi.org/10.1139/cjfr-2020-0433

Dandois, J. P., & Ellis, E. C. (2013). High spatial resolution three-dimensional mapping of vegetation spectral dynamics using computer vision. *Remote Sensing of Environment*, *136*, 259–276. https://doi.org/10.1016/j.rse.2013.04.005

Dandois, J. P., Olano, M., & Ellis, E. C. (2015). Optimal Altitude, Overlap, and Weather Conditions for Computer Vision UAV Estimates of Forest Structure. *Remote Sensing*, *7*(10), 13895–13920. https://doi.org/10.3390/rs71013895

De Luca, G., N. Silva, J. M., Cerasoli, S., Araújo, J., Campos, J., Di Fazio, S., & Modica, G. (2019). Object-Based Land Cover Classification of Cork Oak Woodlands using UAV Imagery and Orfeo ToolBox. *Remote Sensing*, *11*(10), 1238. https://doi.org/10.3390/rs11101238

Díaz, G. M., Mohr-Bell, D., Garrett, M., Muñoz, L., & Lencinas, J. D. (2020). Customizing unmanned aircraft systems to reduce forest inventory costs: Can oblique images substantially improve the 3D reconstruction of the canopy? *International Journal of Remote Sensing*, *41*(9), 3480–3510. https://doi.org/10.1080/01431161.2019.1706200

Farr, T. G., Rosen, P. A., Caro, E., Crippen, R., Duren, R., Hensley, S., Kobrick, M., Paller, M., Rodriguez, E., Roth, L., Seal, D., Shaffer, S., Shimada, J., Umland, J., Werner, M., Oskin, M., Burbank, D., & Alsdorf, D. (2007). The Shuttle Radar Topography Mission. *Reviews of Geophysics*, *45*(2). https://doi.org/10.1029/2005RG000183

Ferraz, A., Bretar, F., Jacquemoud, S., Gonçalves, G., Pereira, L., Tomé, M., & Soares, P. (2012). 3-D mapping of a multi-layered Mediterranean forest using ALS data. *Remote Sensing of Environment*, *121*, 210–223. https://doi.org/10.1016/j.rse.2012.01.020

Frey, J., Kovach, K., Stemmler, S., & Koch, B. (2018). UAV Photogrammetry of Forests as a Vulnerable Process. A Sensitivity Analysis for a Structure from Motion RGB-Image Pipeline. *Remote Sensing*, *10*(6), 912. https://doi.org/10.3390/rs10060912

Gray, A. N., Brandeis, T. J., Shaw, J. D., McWilliams, W. H., & Miles, P. (2012). Forest Inventory and Analysis Database of the United States of America (FIA). *In: Dengler, J.; Oldeland,*

*J.; Jansen, F.; Chytry, M.; Ewald, J., Finckh, M.; Glockler, F.; Lopez-Gonzalez, G.; Peet, R. K.; Schaminee, J .H. J., Eds. Vegetation Databases for the 21st Century. Biodiversity and Ecology. 4: 225-231.*, 225–231. https://doi.org/10.7809/b-e.00079

Hubbell, S. P., Foster, R. B., O'Brien, S. T., Harms, K. E., Condit, R., Wechsler, B., Wright, S. J., & Lao, S. L. de. (1999). Light-Gap Disturbances, Recruitment Limitation, and Tree Diversity in a Neotropical Forest. *Science*, *283*(5401), 554–557. https://doi.org/10.1126/science.283.5401.554

Iglhaut, J., Cabo, C., Puliti, S., Piermattei, L., O'Connor, J., & Rosette, J. (2019). Structure from Motion Photogrammetry in Forestry: A Review. *Current Forestry Reports*, *5*(3), 155–168. https://doi.org/10.1007/s40725-019-00094-3

Jayathunga, S., Owari, T., & Tsuyuki, S. (2018). The use of fixed–wing UAV photogrammetry with LiDAR DTM to estimate merchantable volume and carbon stock in living biomass over a mixed conifer–broadleaf forest. *International Journal of Applied Earth Observation and Geoinformation*, *73*, 767–777. https://doi.org/10.1016/j.jag.2018.08.017

Jeronimo, S. M. A., Kane, V. R., Churchill, D. J., McGaughey, R. J., & Franklin, J. F. (2018). Applying LiDAR Individual Tree Detection to Management of Structurally Diverse Forest Landscapes. *Journal of Forestry*, *116*(4), 336–346. https://doi.org/10.1093/jofore/fvy023

Kellner, J. R., Armston, J., Birrer, M., Cushman, K. C., Duncanson, L., Eck, C., Falleger, C., Imbach, B., Král, K., Krůček, M., Trochta, J., Vrška, T., & Zgraggen, C. (2019). New Opportunities for Forest Remote Sensing Through Ultra-High-Density Drone Lidar. *Surveys in Geophysics*, *40*(4), 959–977. https://doi.org/10.1007/s10712-019-09529-9

Koontz, M. J., Latimer, A. M., Mortenson, L. A., Fettig, C. J., & North, M. P. (2021). Cross-scale interaction of host tree size and climatic water deficit governs bark beetle-induced tree mortality. *Nature Communications*, *12*(1), 129. https://doi.org/10.1038/s41467-020-20455-y

Lamping, J. E., Zald, H. S. J., Madurapperuma, B. D., & Graham, J. (2021). Comparison of

Low-Cost Commercial Unpiloted Digital Aerial Photogrammetry to Airborne Laser Scanning across Multiple Forest Types in California, USA. *Remote Sensing*, *13*(21), 4292. https://doi.org/10.3390/rs13214292

Lasky, J. R., Uriarte, M., Boukili, V. K., Erickson, D. L., Kress, W. J., & Chazdon, R. L. (2014). The relationship between tree biodiversity and biomass dynamics changes with tropical forest succession. *Ecology Letters*, *17*(9), 1158–1167. https://doi.org/10.1111/ele.12322

Li, W., Guo, Q., Jakubowski, M. K., & Kelly, M. (2012). A New Method for Segmenting Individual Trees from the Lidar Point Cloud. *Photogrammetric Engineering & Remote Sensing*, *78*(1), 75–84. https://doi.org/10.14358/PERS.78.1.75

Lin, Y., Hyyppä, J., & Jaakkola, A. (2011). Mini-UAV-Borne LIDAR for Fine-Scale Mapping. *IEEE Geoscience and Remote Sensing Letters*, *8*(3), 426–430. https://doi.org/10.1109/LGRS.2010.2079913

Lisein, J., Pierrot-Deseilligny, M., Bonnet, S., & Lejeune, P. (2013). A Photogrammetric Workflow for the Creation of a Forest Canopy Height Model from Small Unmanned Aerial System Imagery. *Forests*, *4*(4), 922–944. https://doi.org/10.3390/f4040922

Mlambo, R., Woodhouse, I. H., Gerard, F., & Anderson, K. (2017). Structure from Motion (SfM) Photogrammetry with Drone Data: A Low Cost Method for Monitoring Greenhouse Gas Emissions from Forests in Developing Countries. *Forests*, *8*(3), 68. https://doi.org/10.3390/f8030068

Mohan, M., Silva, C., Klauberg, C., Jat, P., Catts, G., Cardil, A., Hudak, A., & Dia, M. (2017). Individual tree detection from unmanned aerial vehicle (UAV) derived canopy height model in an open canopy mixed conifer forest. *Forests*, *8*(9), 340. https://doi.org/10.3390/f8090340

Nesbit, P. R., & Hugenholtz, C. H. (2019). Enhancing UAV–SfM 3D Model Accuracy in High-Relief Landscapes by Incorporating Oblique Images. *Remote Sensing*, *11*(3), 239. https://doi.org/10.3390/rs11030239

Ni, W., Sun, G., Pang, Y., Zhang, Z., Liu, J., Yang, A., Wang, Y., & Zhang, D. (2018). Mapping Three-Dimensional Structures of Forest Canopy Using UAV Stereo Imagery: Evaluating Impacts of Forward Overlaps and Image Resolutions With LiDAR Data as Reference. *IEEE Journal of Selected Topics in Applied Earth Observations and Remote Sensing*, *11*(10), 3578–3589. https://doi.org/10.1109/JSTARS.2018.2867945

North, M. P., Kane, J. T., Kane, V. R., Asner, G. P., Berigan, W., Churchill, D. J., Conway, S., Gutiérrez, R. J., Jeronimo, S., Keane, J., Koltunov, A., Mark, T., Moskal, M., Munton, T., Peery, Z., Ramirez, C., Sollmann, R., White, A., & Whitmore, S. (2017). Cover of tall trees best predicts California spotted owl habitat. *Forest Ecology and Management*, *405*, 166–178. https://doi.org/10.1016/j.foreco.2017.09.019

North, M. P., York, R. A., Collins, B. M., Hurteau, M. D., Jones, G. M., Knapp, E. E., Kobziar, L., McCann, H., Meyer, M. D., Stephens, S. L., Tompkins, R. E., & Tubbesing, C. L. (2021). Pyrosilviculture Needed for Landscape Resilience of Dry Western United States Forests. *Journal of Forestry*, *119*(5), 520–544. https://doi.org/10.1093/jofore/fvab026

Over, J.-S. R., Ritchie, A. C., Kranenburg, C. J., Brown, J. A., Buscombe, D. D., Noble, T., Sherwood, C. R., Warrick, J. A., & Wernette, P. A. (2021). Processing coastal imagery with Agisoft Metashape Professional Edition, version 1.6—Structure from motion workflow documentation. In *Processing coastal imagery with Agisoft Metashape Professional Edition, version 1.6—Structure from motion workflow documentation* (USGS Numbered Series No. 2021–1039; Open-File Report, Vols. 2021–1039, p. 46). U.S. Geological Survey. https://doi.org/10.3133/ofr20211039

Plowright, A. (2021). *ForestTools: Analyzing Remotely Sensed Forest Data*. Comprehensive R Archive Network (CRAN). https://CRAN.R-project.org/package=ForestTools

Popescu, S. C., & Wynne, R. H. (2004). Seeing the Trees in the Forest. *Photogrammetric Engineering & Remote Sensing*, *70*(5), 589–604. https://doi.org/10.14358/PERS.70.5.589

Puliti, S., Solberg, S., & Granhus, A. (2019). Use of UAV photogrammetric data for estimation of biophysical properties in forest stands under regeneration. *Remote Sensing*, *11*(3), 233. https://doi.org/10.3390/rs11030233

Rodman, K. C., Veblen, T. T., Saraceni, S., & Chapman, T. B. (2019). Wildfire activity and land use drove 20th-century changes in forest cover in the Colorado front range. *Ecosphere*, *10*(2), e02594. https://doi.org/10.1002/ecs2.2594

Roussel, J.-R. (2021a, May 20). *Airborne LiDAR Data Manipulation and Visualization for Forestry Applications [R package lidR version 3.0.4]*. Comprehensive R Archive Network (CRAN). https://CRAN.R-project.org/package=lidR

Roussel, J.-R. (2021b, May 20). *Extra functions and algorithms for lidR package [R package lidRplugins version 0.2.0]*. https://github.com/Jean-Romain/lidRplugins

Safford, H. D., & Stevens, J. T. (2017). Natural range of variation for yellow pine and mixed-conifer forests in the Sierra Nevada, southern Cascades, and Modoc and Inyo National Forests, California, USA. *Gen. Tech. Rep. PSW-GTR-256. Albany, CA: U.S. Department of Agriculture, Forest Service, Pacific Southwest Research Station. 229 p.*, *256*. https://www.fs.usda.gov/treesearch/pubs/55393

Sankey, T., Donager, J., McVay, J., & Sankey, J. B. (2017). UAV lidar and hyperspectral fusion for forest monitoring in the southwestern USA. *Remote Sensing of Environment*, *195*, 30–43. https://doi.org/10.1016/j.rse.2017.04.007

Shin, P., Sankey, T., Moore, M. M., & Thode, A. E. (2018). Evaluating Unmanned Aerial Vehicle Images for Estimating Forest Canopy Fuels in a Ponderosa Pine Stand. *Remote Sensing*, *10*(8), 1266. https://doi.org/10.3390/rs10081266

Silva, C. A., Hudak, A. T., Vierling, L. A., Loudermilk, E. L., O'Brien, J. J., Hiers, J. K., Jack, S. B., Gonzalez-Benecke, C., Lee, H., Falkowski, M. J., & Khosravipour, A. (2016). Imputation of Individual Longleaf Pine (Pinus palustris Mill.) Tree Attributes from Field and LiDAR Data. *Canadian Journal of Remote Sensing*, *42*(5), 554–573.

https://doi.org/10.1080/07038992.2016.1196582

Swayze, N. C., Tinkham, W. T., Vogeler, J. C., & Hudak, A. T. (2021). Influence of flight parameters on UAS-based monitoring of tree height, diameter, and density. *Remote Sensing of Environment*, *263*, 112540. https://doi.org/10.1016/j.rse.2021.112540

Tinkham, W. T., & Swayze, N. C. (2021). Influence of Agisoft Metashape Parameters on UAS Structure from Motion Individual Tree Detection from Canopy Height Models. *Forests*, *12*(2), 250. https://doi.org/10.3390/f12020250

Torresan, C., Carotenuto, F., Chiavetta, U., Miglietta, F., Zaldei, A., & Gioli, B. (2020). Individual Tree Crown Segmentation in Two-Layered Dense Mixed Forests from UAV LiDAR Data. *Drones*, *4*(2), 10. https://doi.org/10.3390/drones4020010

Torres-Sánchez, J., López-Granados, F., Borra-Serrano, I., & Peña, J. M. (2018). Assessing UAV-collected image overlap influence on computation time and digital surface model accuracy in olive orchards. *Precision Agriculture*, *19*(1), 115–133. https://doi.org/10.1007/s11119-017-9502-0

USDA Forest Service. (2016). *Forest Inventory and Analysis Strategic Plan FS-1079*. https://www.fia.fs.fed.us/library/bus-org-documents/docs/strategic-plan-docs/FIA%20Strategic%20Plan%20FS-1079.pdf

USGS. (2017). *Unmanned Aircraft Systems Data Post-Processing: Structure-from-Motion Photogrammetry*. National Unmanned Aircraft Systems (UAS) Project Office. https://uas.usgs.gov/nupo/pdf/PhotoScanProcessingDSLRMar2017.pdf

USGS. (2018). *3DEP products and services: The National Map, 3D Elevation Program, https://nationalmap.gov/3DEP/*.

Weinstein, B. G., Marconi, S., Bohlman, S. A., Zare, A., Singh, A., Graves, S. J., & White, E. P. (2021). A remote sensing derived data set of 100 million individual tree crowns for the National Ecological Observatory Network. *ELife*, *10*, e62922. https://doi.org/10.7554/eLife.62922

Weinstein, B. G., Marconi, S., Bohlman, S. A., Zare, A., & White, E. P. (2020). Cross-site learning in deep learning RGB tree crown detection. *Ecological Informatics*, *56*, 101061. https://doi.org/10.1016/j.ecoinf.2020.101061

Westoby, M. J., Brasington, J., Glasser, N. F., Hambrey, M. J., & Reynolds, J. M. (2012). 'Structure-from-Motion' photogrammetry: A low-cost, effective tool for geoscience applications. *Geomorphology*, *179*, 300–314. https://doi.org/10.1016/j.geomorph.2012.08.021

Whittaker, R. H. (1956). Vegetation of the Great Smoky Mountains. *Ecological Monographs*, *26*(1), 1–80. https://doi.org/10.2307/1943577

Wright, S. J., Kitajima, K., Kraft, N. J. B., Reich, P. B., Wright, I. J., Bunker, D. E., Condit, R., Dalling, J. W., Davies, S. J., Díaz, S., Engelbrecht, B. M. J., Harms, K. E., Hubbell, S. P., Marks, C. O., Ruiz-Jaen, M. C., Salvador, C. M., & Zanne, A. E. (2010). Functional traits and the growth–mortality trade-off in tropical trees. *Ecology*, *91*(12), 3664–3674. https://doi.org/10.1890/09-2335.1

Xiao, W., Zaforemska, A., Smigaj, M., Wang, Y., & Gaulton, R. (2019). Mean Shift Segmentation Assessment for Individual Forest Tree Delineation from Airborne Lidar Data. *Remote Sensing*, *11*(11), 1263. https://doi.org/10.3390/rs11111263

Yancho, J. M. M., Coops, N. C., Tompalski, P., Goodbody, T. R. H., & Plowright, A. (2019). Fine-Scale Spatial and Spectral Clustering of UAV-Acquired Digital Aerial Photogrammetric (DAP) Point Clouds for Individual Tree Crown Detection and Segmentation. *IEEE Journal of Selected Topics in Applied Earth Observations and Remote Sensing*, *12*(10), 4131–4148. https://doi.org/10.1109/JSTARS.2019.2942811

Young, D., Alex, Alexander, MallikaNocco, & Hereñú, D. (2021). *ucdavis/metashape: V0.1.0*. Zenodo. https://doi.org/10.5281/zenodo.5088962

Young, D. J. N., Koontz, M. J., & Weeks, J. (2021). *Open Science Framework repository: Optimizing aerial imagery collection and processing parameters for drone-based*

*individual tree mapping in structurally complex conifer forests*. https://doi.org/10.17605/OSF.IO/KB3NJ

Young, D., Meyer, M., Estes, B., Gross, S., Wuenschel, A., Restaino, C., & Safford, H. D. (2020). Forest recovery following extreme drought in California, USA: Natural patterns and effects of pre-drought management. *Ecological Applications*, *30*(1), e02002. https://doi.org/10.1002/eap.2002

Zaforemska, A., Xiao, W., & Gaulton, R. (2019). INDIVIDUAL TREE DETECTION FROM UAV LIDAR DATA IN A MIXED SPECIES WOODLAND. *ISPRS - International Archives of the Photogrammetry, Remote Sensing and Spatial Information Sciences*, *XLII-2/W13*, 657–663. https://doi.org/10.5194/isprs-archives-XLII-2-W13-657-2019